Wake-induced lateral migration of approaching bubbles

Wake-induced lateral migration of approaching bubbles

Hiroaki Kusuno[a,*], Toshiyuki Sanada[a]

[a] Department of Mechanical Engineering, Shizuoka University, 3-5-1 Johoku Naka-Ku Hamamatsu Shizuoka, 432-8561 Japan

*corresponding author

E-mail: kusuno.hiroaki.17@shizuoka.ac.jp, sanada.toshiyuki@shizuoka.ac.jp

Abstract

In the motion of two gravity-driven bubbles arranged in a line, the trailing bubble is known to accelerate in the wake of the leading bubble. Furthermore, the approaching bubble migrates laterally as a result of bubble–bubble interactions. This paper presents the physical mechanisms for the acceleration and lateral motions of deformable bubbles under stable conditions, i.e., rectilinear motion in a solitary bubble, using numerical simulations. First, the trailing bubble decreases the drag coefficient relative to the case of a spherical bubble as a result of the increased vorticity generated at the leading bubble surface by its deformation. Second, the trailing bubble moves laterally as a result of the shear-induced lift force. In addition, lift reversal occurs in high Bond number cases and very weak lift occurs in low Galilei number cases. Predictions under the assumption of spherical bubbles nearly reproduce the interaction of a pair of deformable bubbles; however, the motion associated with the lift reversal cannot be predicted. Third, the bubbles repel each other as a result of their potential interaction when they are adjacent. This repulsive interaction is due to both the pressure at the surface and the vortex interaction around the bubbles.

Keywords: bubble–bubble interaction, bubble wake, bubble deformation, repulsive force, lift reversal, vortex ring

1. Introduction

The hydrodynamic interactions between bubbles rising in a viscous liquid are fundamental factors in determining the structure of bubbly flow, including the local void fraction and the distribution of the bubble diameters. Local void fractions have been experimentally observed (Prakash et al. 2016). In particular, horizontal clusters have been experimentally observed in two-dimensional bubbly flows resulting from wall interactions (Sangani et al. 2001; Takagi et al. 2008). Therefore, it is necessary to understand the motions of bubbles when they interact to predict the development of a bubbly flow. The various aspects of the interaction between two bubbles, such as bubbles rising in line, are unknown despite their simplified interaction, that is, compared to the interactions of multiple bubbles that arise in various industrial applications.

Assuming irrotational flow, Levich (1962) theoretically derived the drag force of a spherical bubble according to the kinetic energy balance. This assumption is reasonable in nearly all regions except at the boundary layer of the bubble surface, where vorticity is generated as a result of the curvature even for zero shear stress conditions, and in the wake as a result of the advection of vorticity from the surface (Moore 1963). Based on the potential flow model, Kok (1993) theoretically derived the interaction between two spherical bubbles and found that the bubbles attract each other when the angle between their centerlines and the direction of motion is in the range of 0° to 180° $- \theta_c$, where θ_c is a critical angle ranged from 35° to 54.7°; otherwise, the bubbles repel each other. Therefore, repulsion is an in-line bubble interaction.

Direct numerical simulations by Yuan and Prosperetti (1994), in which the Reynolds number ($Re = \rho U d/\mu$) ranged from 50 to 200, disagreed with potential flow predictions because the effect of the wake of the leading bubble (hereinafter referred to as B1) is an important factor that attracts the trailing bubble (hereinafter referred to as B2) when bubbles rise in line. They demonstrated the existence of an equilibrium distance S_e normalized by the radius, where the potential repulsive force balances the wake attractive effect:

$$S_e = 4.4 \log_{10} Re - 4.38. \tag{1}$$

Considering the effect of the vorticity generated at the surface of B1 and its advection and diffusion in the wake of B2, Harper (1997) recalculated his previous analytical model (Harper, 1970) and found results in good agreement with the numerical results.

In the numerical simulation results of Watanabe and Sanada (2006), the Bond number $(Bo = \rho d^2 g/\sigma)$ is 0.00878, predicting a reduction in the equilibrium distance resulting from the bubble deformation. In addition, they performed experiments employing silicone oils ($5 \le Re \le 40$) and found different interesting interactions, including collisions, equilibrium distances greater than the numerical results, and escapes from the rising line. Hallez and Legendre (2011) computed the three-dimensional (3D) flow around two fixed spherical bubbles ($20 \le Re \le 500$) and simulated general cases in which the positions of the bubbles were not arranged. They found another important effect of the wake, a transverse effect due to shear flow. In the wake, the transverse effect is similar to the lift force F_L of a solitary bubble in a linear shear flow (Auton 1987; Legendre and Magnaudet 1998):

$$F_L = C_L(\pi d^3/6)\rho U \times (\nabla \times \boldsymbol{u}), \tag{2}$$

where C_L is the lift coefficient, $\boldsymbol{u}$ is the fluid velocity, and $(\nabla \times \boldsymbol{u})$ corresponds to the vorticity in the wake. The lateral migration of B2 was experimentally observed by Kusuno and Sanada (2015) for bubbles rising in pure water ($50 \le Re \le 300$). They found that B2 escapes from the rising line immediately after the bubble is generated and predicted that this was caused by the shear-induced lift because a solitary bubble rose stably under the same conditions. Consequently, they never observed the equilibrium distance for a combination of the potential effect and the wake effect. The 3D simulations using a volume of fluid (VOF) method by Gumulya et al. (2017) indicated that the development of the vorticity around B2 due to the acceleration causes the escaping from the original line ($50 < Re$). More recently, Kusuno et al. (2019) performed a series of experiments employing silicone oil ($20 \le Re \le 60$). They observed the relative motions of the bubbles and found collisions at low Re and escapes from the rising line at intermediate Re. Interestingly, B1 was repelled vertically and horizontally at short separation distances, even though the bubbles rarely came into contact according to images from a high-speed video camera with a 0.084-mm/pixel resolution. Accordingly, they predicted that the repulsive interaction was a potential hydrodynamic effect.

Visualization of the flow fields was not performed by Kusuno et al. (2019), and important parameters, such as the velocity and the vortex structure, around the interacting bubbles are unknown. In particular, the vortex structure dominates the characteristics of the bubble rising path. The pair of counter-rotating threads in the wake of a solitary bubble induces a zigzag or spiral path (Tripathi et al. 2015; Cano-Lozano et al. 2016; Zhang and Ni 2017). The thread pairs also appear behind the bubble, acting on the shear-induced lift force in a linear shear flow (Magnaudet and Eames 2000). As a consequence, the structure of the flow behind each bubble is also important for its interactions.

In this study, a pair of 3D bubbles rising in line is numerically computed using the open-source code Basilisk (Popinet, S) with an adaptive VOF method, as sketched in Figure 1. The target range of the Galilei number ($Ga = \rho d^{3/2} g^{1/2}/\mu$) and Bo is based on a previous experimental study by Kusuno et al. (2019), and the mapping of the conditions onto the phase diagram in the (Ga, Bo) plane proposed by Cano-Lozano et al. (2016) is shown in Figure 2. We divide the interactions between the two bubbles into the following: the vertical attraction of B2, the transverse repulsion of B2, and the vertical/transverse repulsion of both bubbles. To examine the physical mechanisms underlying the attractive/repulsive motion, we investigate the forces acting on the surfaces of the bubbles, the vortex structure, and their couplings for each case. The main focuses in the present study are, first, the deformation effect connected to the approaching bubble, second, whether the lateral migration of B2 occurs as a result of the shear-induced lift or the bubble-velocity-induced lift, and third, why the two bubbles repel each other. We analyze the motions of the bubbles, pressure and normal viscous stress at the surface, and vortical flow structure, including the vorticity and the invariants of the velocity-gradient tensor λ_2 (Jeong and Hussain 1995), around the bubbles to discuss the above points.

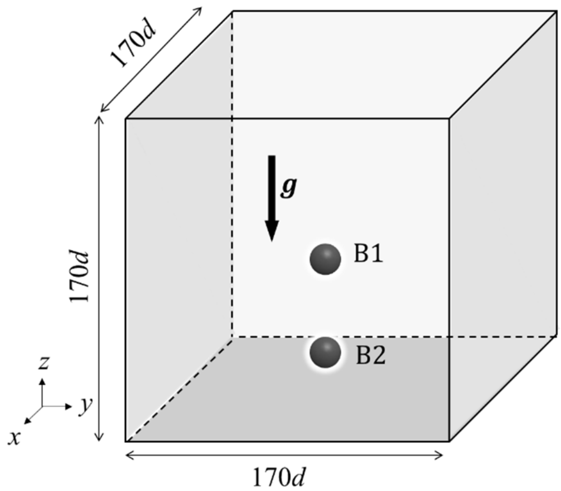

Fig. 1. The computational domain of a pair of gravity-driven bubbles. The domain is 170 times the bubble diameter allowing the boundary effects to be neglected.

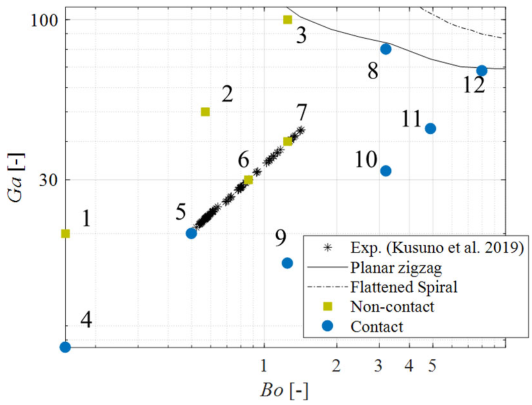

Fig. 2. Mapping of the numerical conditions for the current study onto a phase diagram in the *Ga*–*Bo* plane proposed by Cano-Lozano et al. (2016). All the conditions are near those of the experimental results (Kusuno et al. 2019) and under stable bubble conditions (rectilinear motion in a single bubble).

2. Methods

2.1 Numerical method

We considered a pair of gravity-driven spherical bubbles in a container, as shown in Figure 1. The initial positions were on the centerline or slightly deviated from the centerline, as shown in Figures 3(a) and 3(b). To enable the boundary effect to be neglected, the domain was 170 d × 170 d × 170 d, where d corresponds to the diameter of the bubbles. The x–y plane was the horizontal plane, and the z-direction was in the direction of gravity and was perpendicular to the x–y plane. Table 1 provides a list of the numerical conditions.

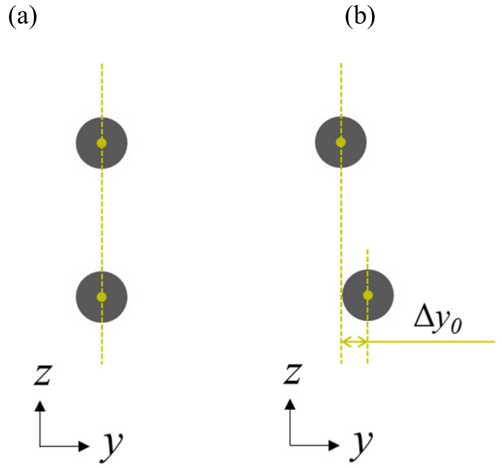

Fig. 3. Initial positions of a pair of bubbles.

Table 1. Numerical conditions corresponding to Figure 2.

Case	*Ga*	*Bo*	*Re*	Δy_0	Aspect ratio	Contact	Lift coefficient (Hayashi et al.,2020)
1	20	0.15	20	0	1.0	No	0.37
2	50	0.57	81	0	1.2	No	0.42
3	100	1.25	165	0	1.7	No	0.18
4	8	0.15	4.6	0	1.0	Yes	0.36
5	20	0.5	20	0	1.1	Yes	0.28
6	30	0.86	36	0	1.2	No	0.37
7a	40	1.25	52	0	1.3	No	0.34
7b	40	1.25	52	0.1	1.3	No	0.34
8	80	3.2	98	0	2.1	Yes	-0.30
9	16	1.25	13	0	1.1	Yes	0.30
10	32	3.2	32	0	1.5	Yes	0.08
11	44	4.9	43	0	1.8	Yes	-0.16
12a	68	8	62	0	2.6	Yes	-0.67
12b	68	8	62	0.5	2.6	Yes	-0.67

We used the open-source code Basilisk, which was developed by the same author who developed the Gerris flow solver (Popinet 2003, 2009), to calculate the incompressible, variable-density, Navier–Stokes equations:

$$\nabla \cdot \boldsymbol{u} = 0, \tag{3}$$

$$\rho[\partial \boldsymbol{u}/\partial t + \boldsymbol{u} \cdot \nabla \boldsymbol{u}] = -\nabla p + \nabla \cdot (2\mu \boldsymbol{D}) + \sigma\kappa\delta\boldsymbol{n} + \rho\boldsymbol{g}, \tag{4}$$

where $\boldsymbol{D} = [\nabla\boldsymbol{u} + (\nabla\boldsymbol{u})^T]/2$ is the deformation tensor, σ is the surface tension coefficient, κ is the curvature of the interface, δ is the Dirac distribution function, $\boldsymbol{n}$ is the unit vector normal to the interface, and $\boldsymbol{g}$ is the gravity. The spatial gradient calculation is second order, and the time advancement uses a second-order fractional-step method with a staggered discretization.

The interface was tracked using a geometric VOF method. The advection of the volume fraction field is written as

$$\partial c/\partial t + \nabla \cdot (c\boldsymbol{u}) = 0, \tag{5}$$

where c is the volume fraction. The density and viscosity at each cell are calculated as a function of c:

$$\rho = c\rho_1 + (1-c)\rho_2, \tag{6}$$

$$1/\mu = c/\mu_1 + (1-c)/\mu_2, \tag{7}$$

where ρ_1, ρ_2 and μ_1, μ_2 are the densities and viscosities of each fluid, respectively. The density and viscosity ratios were 900 and 300, respectively.

The grid resolution is important to determine the accuracy of the bubble motion and the flow around the bubbles (Blanco and Magnaudet 1995; Magnaudet and Mougin 2007). The velocity field in the viscous boundary layer, which is the origin of the wake, needs to be calculated accurately because the wake of B1 affects the motion of B2 according to multiple previous studies (e.g., Yuan and Prosperetti 1994; Hallez and Legendre 2011). Kusuno and Sanada (2020), who computed the axisymmetric flow around a solitary bubble, compared the velocity profiles using a boundary fitted coordinate system (BFC) and a Cartesian coordinate system using the VOF method. They found that 4 points are required within the critical distance (where the critical distance is $\sqrt{(Re+75)/[Re(Re-5)]}$ on the side of a spherical bubble) to make accurate computations using VOF because the sign of the tangential velocity gradient for the radial direction $\partial u_t/\partial r$ reverses in the boundary layer. For example, in Case 3, which is the numerically toughest condition, the critical distance (the distance is approximately boundary layer thickness) is 0.097d. Based on their study, we set 96 cells within the bubble diameter in this study. At low *Re* numbers, we set 48 cells within the bubble diameter because of the computational cost. The grid size accurately calculates the pressure-velocity field in the boundary layer. Note that, according to Zhang et al. (2019), this resolution is not sufficient to compute the bubble coalesce/bounce accurately.

An adaptive mesh refinement method can lower the computational cost (Cano-Lozano et al. 2016). We used a wavelet decomposition of the volume fraction and the velocity fields to refine the mesh. We believe that the velocity criterion, which is sensitive to the second derivative of the velocity fields, is suitable to calculate relevant fields of a rising bubble because the reversal sign of the velocity gradient is in the boundary layer where the grid resolution is high. The error threshold was set to 0.005.

We also investigated the force acting on a bubble surface induced by the flow field. However, the calculation points and the bubble surface do not match. According to Kusuno and Sanada (2020), the 5th order extrapolation pressure and velocity at the surface obtained by the VOF method with an accurate pressure-velocity field agree with the BFC method, which calculates the value at the surface directly. The grid size in the current research is sufficient to obtain the accurate pressure-velocity field. Therefore, we used 5th order extrapolation in the liquid phase to estimate the bubble surface pressure and velocity. The expected velocity and pressure errors are less than 1% and 3%, respectively.

2.2 Forces acting on the bubble

To investigate the details of the bubble interactions, it is necessary to conduct comparisons with previous studies. One general quantitative evaluation involves a comparison of the drag coefficient and the lift coefficient. We adopted the method used in Shew et al. (2006) based on the generalized Kirchhoff equations (Howe 1995; Mouguin and Magnaudet 2002) to derive the drag and lift coefficients of each bubble. Assuming two-dimensional plane motion (zero spiral motion), an axisymmetric shape, and that the minor axis of the bubble is nearly aligned with its velocity (Mouguin and Magnaudet 2001; De Vries et al. 2002, Shew et al. 2006), these equations can be reduced to

$$\rho V A_{11}\, dU_1/dt = F_D + F_{B1}, \tag{8}$$

$$\Omega_3 \rho V A_{11} U_1 = F_L + F_{B2}, \tag{9}$$

where A_{11} is the added mass inertia tensor, $\Omega_3 = d\theta/dt$ is the angular velocity, F_D is the drag force, and F_B is the buoyant force. The bubble orientation is (1, 2, 3), as shown in Figure 4. The centers of both bubbles are in the (1, 2) plane. A_{11} of a solitary bubble is a function of the bubble aspect ratio χ (Lamb 1945; Kochin et al. 1964), with a simplified linearization of (Klaseboer et al., 2001)

$$A_{11} \cong 0.62\chi - 0.12 \text{ for } 1 \leq \chi. \tag{10}$$

We selected Eq. (10) to estimate the drag and lift coefficients. Note that the total added mass of the two spherical bubbles A_{sum} estimated by the kinetic energy is a function of the relative distance given by $A_{sum} = 1 + S^{-3}[-3/4 - 9/4\cos(2\theta)]$. For adjoining bubbles where S ~ 2, the added mass of the bubbles varies by approximately 30% from that of a solitary bubble. The variable added mass effect on the drag and lift coefficients is smaller than 12% because the buoyant force is greater than the added mass force.

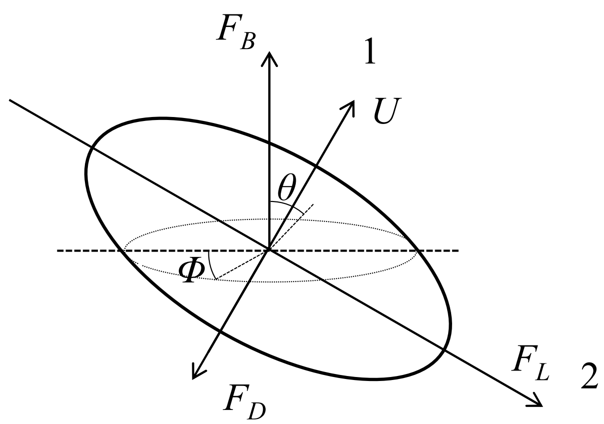

Fig. 4. Definition of the bubble orientation: 1 and 2 indicate the rising and lift directions, respectively, while θ and Φ indicate the tangential and azimuthal angles, respectively.

3. Results and discussion

3.1 Comparison of bubble trajectories with previous experiments

We computed the motions of pairs of bubbles under various conditions, as shown in Table 1. We set the position to be in line or slightly out of line to reproduce the experimental conditions. We first confirmed the motion of the bubbles and then investigated the interaction mechanisms.

Figure 5(a) shows the temporal change in the velocities for each bubble, Figure 5(b) shows the relative trajectory, and Figure 5(c) shows the image sequence of the bubbles at Ga = 40 and Bo = 1.25 (Case 7a in Table 1), where the initial position was in line. At first, the rising velocity of B2 is greater than that of B1 at times (i) and (ii), corresponding to $t \sim 0$–25. The velocity of B1 is nearly the same as that of a solitary bubble, and that of B2 is fast enough to catch up with B1. Because the relative distance is large, the acceleration of B2 results from the interaction with the wake of the leading bubble, as found in previous studies (Yuan and Prosperetti 1994; Harper 1997; Hallez and Legendre 2011; Kusuno et al. 2019). The lift force does not act on either bubble during this period, and B2 approaches B1 from the rear. Then, the velocity of B1 increases at time (ii), corresponding to $t \sim 25$ and $S \sim 2.6$. Assuming an axisymmetric flow around the two spherical bubbles, the bubbles should maintain an equilibrium distance as a result of the balance between the potential and wake effects (Yuan and Prosperetti 1994; Harper 1997). The bubbles approach each other up to S = 2.6, but the equilibrium distance S_e, estimated by Eq. 1, is 3.1 at Ga = 40 (Re = 50). Our numerical distance is shorter than the numerically obtained equation under the spherical bubbles assumption. This tendency is the same as that found in axisymmetric numerical results considering deformation (Watanabe and Sanada 2006).

(a)

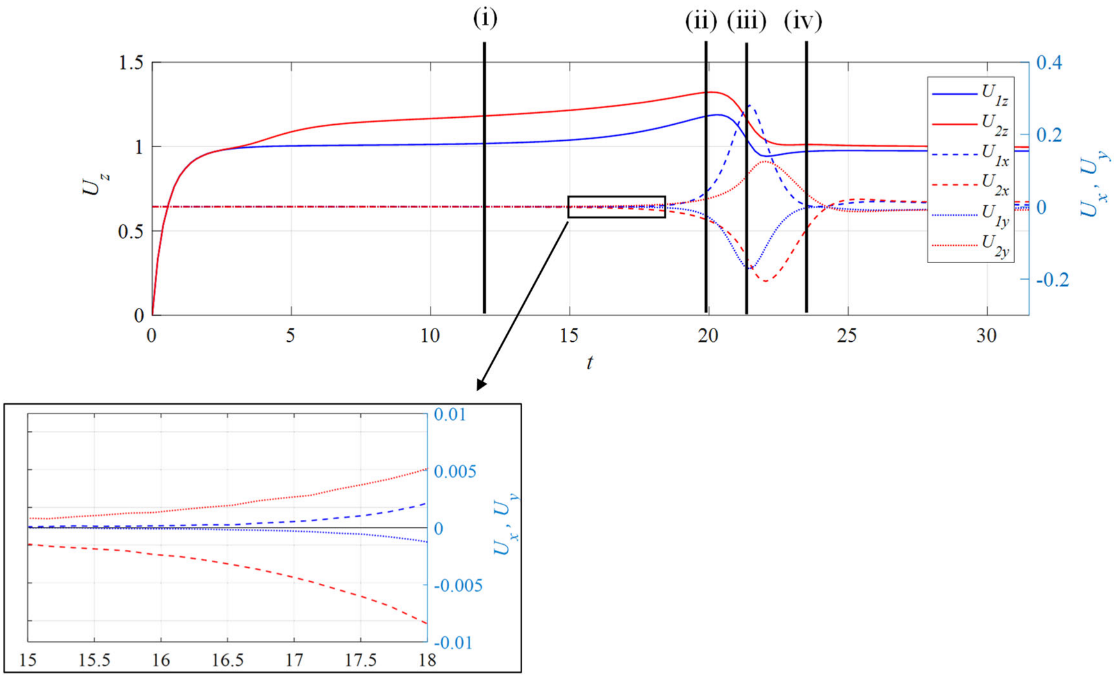
(i)
(ii)
(iii)
(iv)
U_z
t
U_x, U_y
U_{1z}
U_{2z}
U_{1x}
U_{2x}
U_{1y}
U_{2y}

(b)

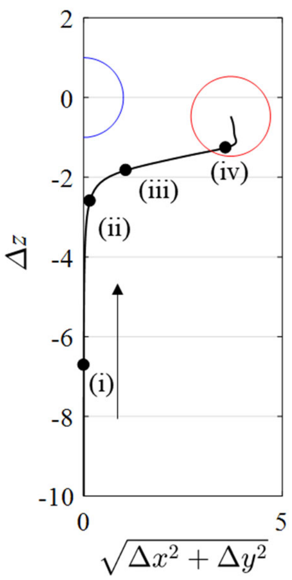
Δz
$\sqrt{\Delta x^2 + \Delta y^2}$
(i)
(ii)
(iii)
(iv)

(c)

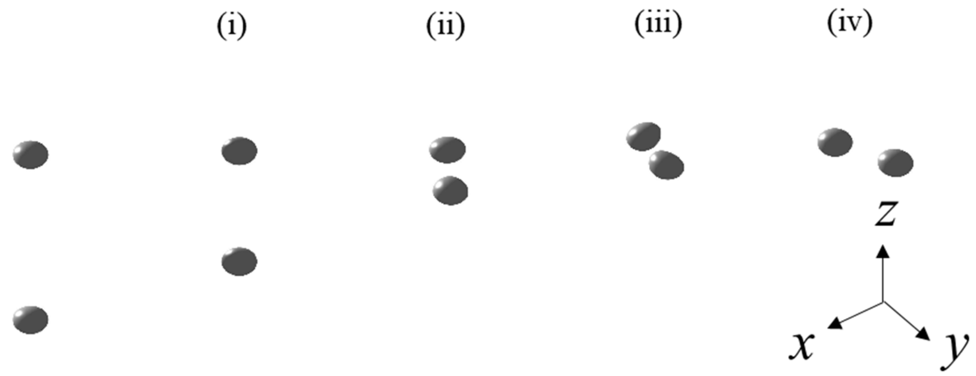

Fig. 5. Time advancement of the bubble motion (Ga = 40, Bo = 1.25, Case 7a in Table 1): (a) bubble velocity; (b) relative trajectory of B2; and (c) motion of both bubbles, where the reference frame follows that of the rising velocity of a solitary bubble, at the following times: (i) B2 accelerated by the wake of B1, (ii) onset of repulsion of the two bubbles, (iii) maximum repulsion of the two bubbles, and (iv) weakened mutual repulsive interaction.

After the acceleration of the two bubbles, the bubbles repel each other in the transverse direction at times (ii)–(iv), corresponding to t ~ 25–30. Because the relative distance is small, the repulsion is likely due to the potential effect. This lateral migration can be observed in experiments (Watanabe and Sanada 2006; Kusuno et al. 2019). Under the condition in Figure 5, the bubbles rarely come into contact; however, they do come into contact under some conditions. Figure 2 shows a summary of contact/non-contact occurrences in the initially positioned in-line case around the experimental conditions: the bubbles come into contact when there is no lateral migration. Within the conditional range of the current numerical study, non-contact occurred at high *Ga* and low *Bo*. Kusuno et al. (2019) stated that bubbles easily deviate from the original line in experiments as a result of asymmetrical disturbances due to the initial relative angle.

We investigated the effect of the initial arrangement. Figure 6 shows the same conditions as in Figure 5 but with the initial position out of line to simulate the experimental conditions ($\Delta y_0 = 0.1a$, Case 7b in Table 1), Figure 6(a) shows the temporal changes in the velocities of each bubble, Figure 6(b) shows the relative trajectories, and Figure 6(c) shows an image sequence of the bubbles at *Ga* = 40 and *Bo* = 1.25. From the figure, it appears that lateral migration occurs more easily under this condition than under the in-line condition. This is because axisymmetry is broken. The lateral migration is caused by the wake effect resulting from the large relative distance. However, it is necessary to discuss whether this migration is due to shear-induced lift or instability, i.e., bubble-velocity-induced lift.

Based on the above results, in the following section, we discuss three topics: (1) if deformable bubbles approach each other more than spherical bubbles, (2) if lateral migration is due to the shear-induced lift or instability, and (3) if the bubbles repel each other. The detailed flow structures obtained from the numerical analysis are then discussed.

(a)

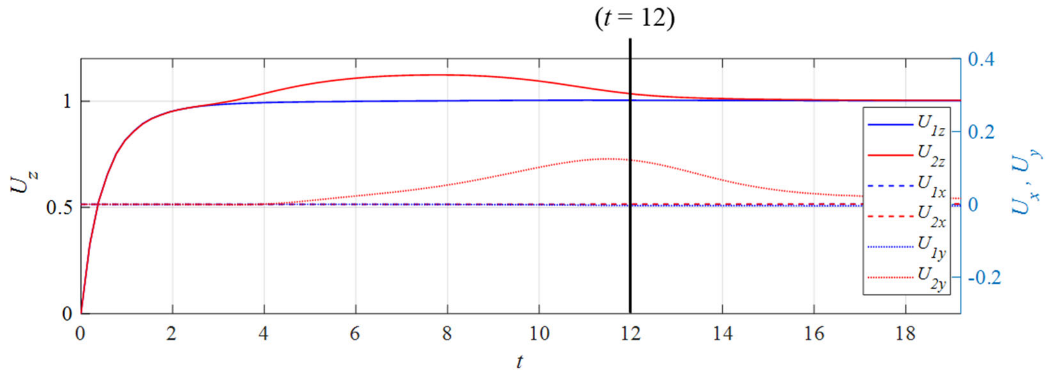

(t = 12)
U_z
U_x, U_y
t
U_{1z}
U_{2z}
U_{1x}
U_{2x}
U_{1y}
U_{2y}

(b)

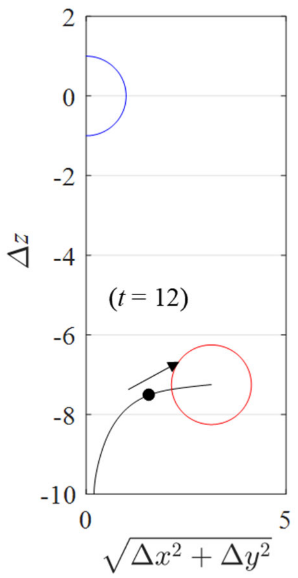

(t = 12)
Δz
$\sqrt{\Delta x^2 + \Delta y^2}$

(c)

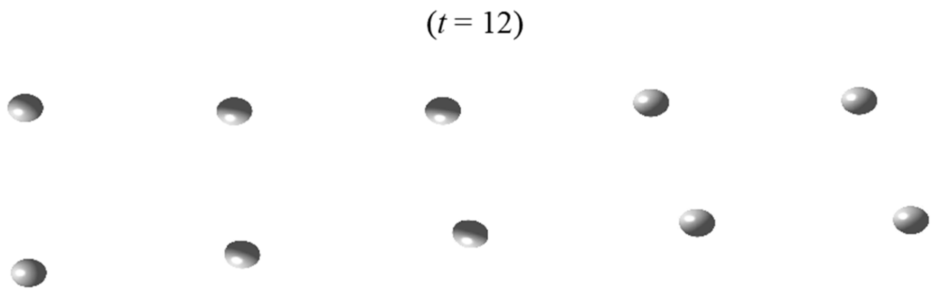

Fig. 6. Progression of the bubble motion through time (*Ga* = 40, *Bo* = 1.25, $\Delta y_0 = 0.1$, Case 7b in Table 1): (a) bubble velocities, (b) relative trajectory of B2, and (c) the motions of the two bubbles (*t* = 12). Only B2 is observed to migrate laterally.

3.2 Acceleration of the trailing bubble

When the two bubbles are positioned in a vertical line, the rise velocity of B2 increases as a result of the wake effect from B1, as shown in Figure 5(a) at time (i). According to Hallez and Legendre (2011), this interaction is a combination of three effects: the potential effect, a viscous correction, and a wake effect. The potential effect is a repulsive force (an increase in the drag force on B2) when the bubbles rise in line. The drag coefficient of B2 increases as the bubbles approach each other because the potential interaction effect is proportional to S^{-4}, e.g., the drag force of the trailing spherical bubble considering the potential flow is written as (Kok 1993; Hallez and Legendre 2011)

$$C_{D2} = 48/Re[1 - 2S^{-3} + \cdots] + 12S^{-4} + \cdots. \quad (11)$$

The relative distance S is approximately 7 at time (i) in Figure 5; therefore, the effect of the potential interaction on B2 is negligibly small.

Based on the above results, we examined the drag coefficient of B2. The interaction components of the drag and lift coefficients are expressed as

$$C_D = C_D^{single} + (C_D^{HL} - C_D^{Moore}),$$

$$C_L = C_L^{HL}, \quad (12)$$

where the superscript “single” indicates an empirical model of the drag coefficient for a deformable single bubble estimated by an experiment (Kusuno et al. 2019), the superscript “HL” indicates the spherical bubbles model proposed by Hallez and Legendre (2011), and the superscript “Moore” indicates the theoretical spherical bubble model derived by Moore (1963). Thus, the left terms are a combination of solitary deformable bubble drag coefficient and spherical bubbles interaction coefficient.

Figure 7(a) shows the total drag coefficients of the bubbles. For B1 at time (i), the total drag coefficient is in good agreement with the drag coefficient C_D^{single} estimated by Kusuno et al. (2019) without interactions. For B2 at time (i), the total drag coefficient decreases as a result of the wake effect but is smaller than that predicted by Eq. (12). The dominant interaction for B1 is the potential effect because the flow upstream of B1 is uniform. However, this effect is minimal because of the large relative distance at time (i). Similarly, the potential effect of B2 is minimal. Therefore, the potential effect could be negligible here. One difference in the computation conditions between the present simulation and that of Hallez and Legendre (2011) is deformation. Because the deformation effect that contributes to the potential effect is small, we consider two causes for the different drag coefficients: the deformation effect on the drag coefficient of B2 and the deformation effect on the vorticity strength of B1.

(a)

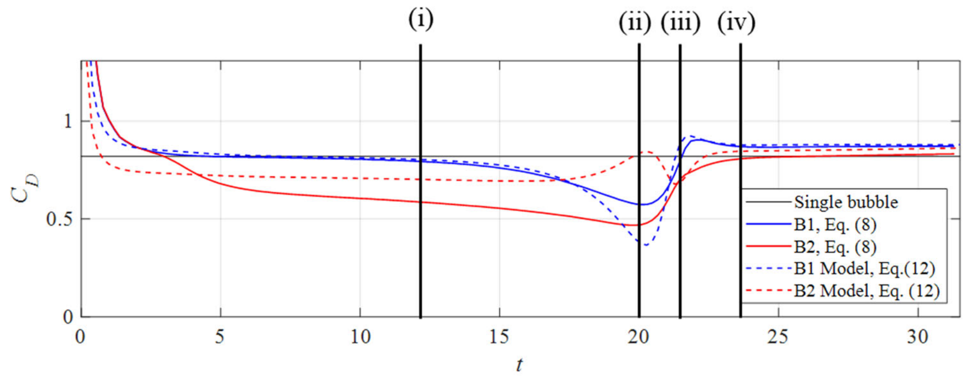

(b)

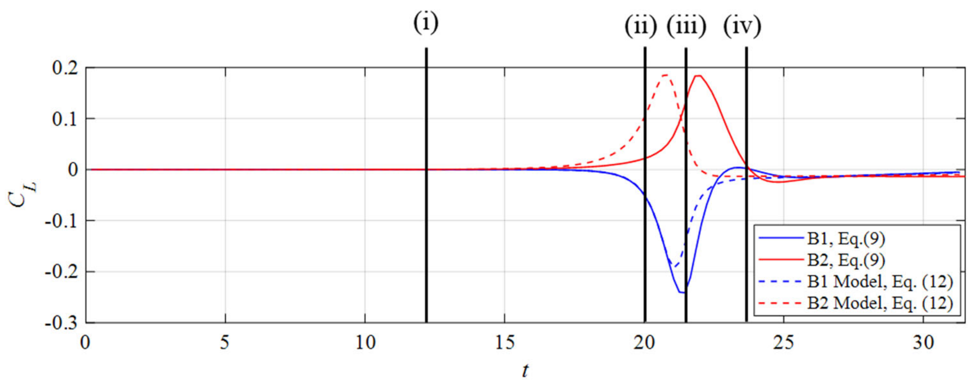

Fig. 7. Comparison of the drag and lift coefficients of the bubbles (Eq. (8)) as predicted by the model (Eq. (12)) (*Ga* = 40, *Bo* = 1.25, Case 7a in Table 1), with times (i)–(iv) corresponding to the times indicated in Figure (5): (a) drag coefficients and (b) lift coefficients.

Figures 8(a), (b), (c), and (d) show the aspect ratio, top and bottom curvature, left and right curvature, and shape of bubbles, respectively. At the time (i), the shape of B1 is the same as a solitary bubble because of the minimal potential interaction. Conversely, the shape of B2 is elongated as a result of the strong wake interaction although Weber number ($We = \rho U^2 d/\sigma$) of B2 is greater than that of B1 due to the velocity of bubbles. Thus, the drag coefficient of B2 is smaller than that of a solitary bubble because of the aspect ratio reduction even if the large *We*.

Also, Figures 8 (b), (c), and (d) show that the shape of the top of B2 is sharp. It is because of the pressure reduction of the wake effect as follows. Figure 9 shows the pressure coefficient and the normal viscous stress at the bubble surface at time (i). The pressure coefficient at the front stagnation point of B2 is smaller than that of B1 as a result of the wake effect of B1 on B2, whereas the flow upstream of B1 is uniform. The integration of the normal pressure reduces the drag force. More interestingly, the pressure at the rear of B2 is close to that of a single bubble. This suggests that the wake of B1 has only a small effect on the rear part of B2. This pressure difference varies the bubble curvature, as shown in Figures 8 because the bubble curvature is determined by balancing the normal stress at the surface. The curvature of B2 is different from that of a single bubble but the bottom of B2 is the same. The curvature of the front of B2 is greater than that of a solitary bubble because the pressure reduction at the front of B2 prevents flatting. The curvature of the side is smaller than that of a solitary bubble because of the tangential velocity reduction due to the wake of B1 (see appendix C). Thus, the maximum vorticity of B2 is smaller than a solitary bubble, the drag force, which is approximately proportional to the maximum vorticity (Legendre, 2007), is expected to be decreased.

(a)

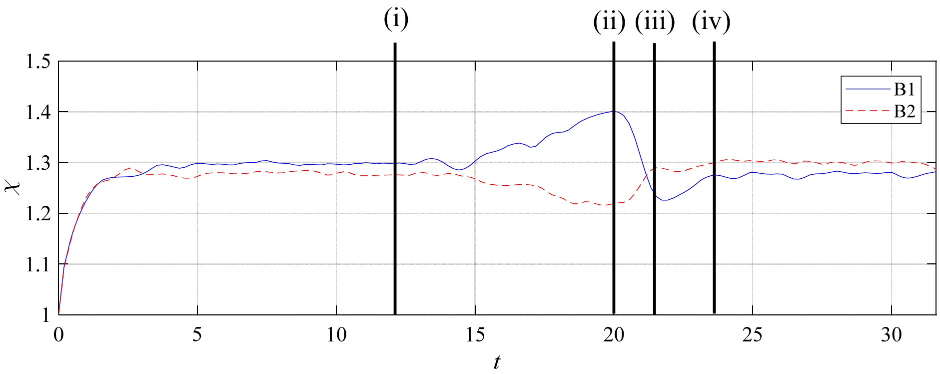

(b)

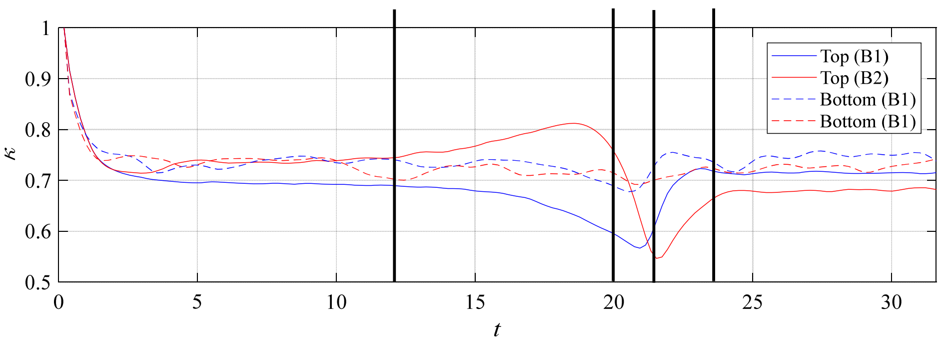

(c)

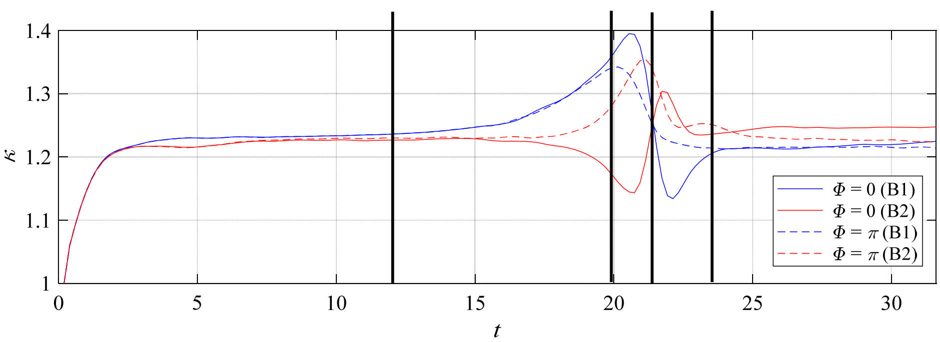

(d)

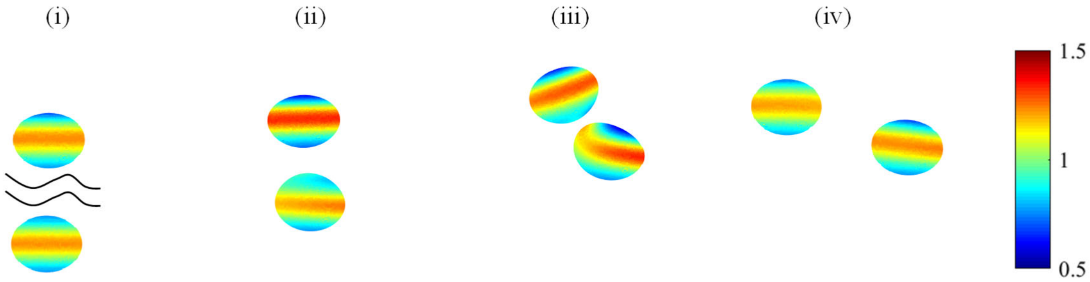

Fig. 8. Progression of bubbles shape through time (*Ga* = 40, *Bo* = 1.25, $\Delta y_0 = 0$, Case 7a in Table 1): (a) aspect ratio, (b) top and bottom curvatures, (c) left and right curvatures, (d) bubbles shape and curvature contour.

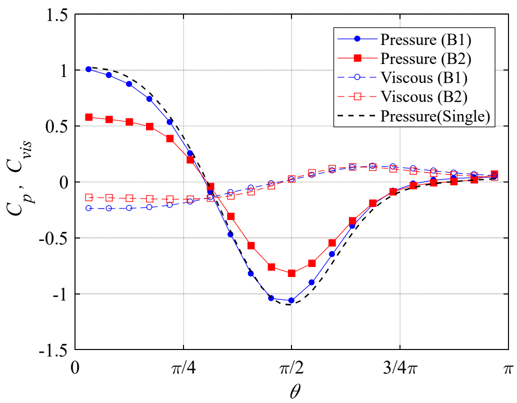

Fig. 9. Pressure coefficient C_p and normal viscous stress coefficient C_{vis} of the bubbles as a function of the angle θ from the center of each bubble at time (i), when B2 is accelerated by the wake of B1 (*Ga* = 40, *Bo* = 1.25, Case 7a in Table 1).

Next, we explain the deformation effect of B1. When a bubble deforms from a spherical shape, the amount of vorticity generated at the bubble surface increases because of the boundary conditions; here, the gas–liquid boundary conditions for the curvature and velocity are that the shear stresses are the same. Because the viscosity of gas is sufficiently smaller than that of a liquid, it can be regarded as zero-shear stress. The gas–liquid boundary condition is $\omega = 2\kappa u$ (Batchelor 1967) for zero-shear stress, and the vorticity is proportional to the curvature and the velocity. A spheroidal bubble has a larger curvature and a higher velocity than a spherical bubble; therefore, its vorticity generation is also larger. The maximum value of vorticity generated at the surface of a spheroidal bubble is expressed as a function of the aspect ratio χ in the infinite *Re* limit (Magnaudet and Mouguin 2007):

$$\omega_{max} = \frac{2U}{a} \frac{\chi^{5/3} (\chi^2 - 1)^{3/2}}{\chi^2 \sec^{-1} \chi - (\chi^2 - 1)^{1/2}}, \tag{13}$$

where ω_{max} is proportional to $\chi^{8/3}$ at very large χ. At low *Re*, the vorticity reaches the simple expression (Legendre, 2007):

$$\omega_{max} = \frac{U}{a} \chi, \tag{14}$$

where ω_{max} is proportional to χ. Our numerical results show the same trend (see appendix C). The wake of the spheroidal bubble, where vorticity increases because of the deformation, reduces the drag force of B2 in comparison to a spherical bubble because the vorticity affects the pressure field. The large deformed bubble (spheroidal bubble) case is discussed in the following section. Even though the wake also increases the normal stress because it decreases the relative velocity between the bubble and the liquid, the pressure is dominant.

3.3 Lateral migration of the trailing bubble

When the two bubbles are initially positioned slightly off the vertical line ($\Delta y_0 = 0.1$), B2 escapes from the original vertical line as a result of the wake effect of B1, as shown in Figure 6. This lift force is due to the shear-induced lift force (Auton 1987; Legendre and Magnaudet 1998; Hallez and Legendre 2011). According to Legendre and Magnaudet (1998), the asymmetric pressure profile dominates the shear-induced lift force at O(10) < *Re*. We checked the pressure coefficient, normal viscous stress coefficient, and velocity at the B2 surface to show the lift force due to pressure at t = 12 in Figure 6; this is shown in Figure 10, where Φ = 0 is between the bubbles on the (1, 2) plane (see Figure 5). The front part of the bubble, where the pressure at Φ = 0 is smaller than at $\Phi = \pi$, has a small effect on the lift force as a result of the normal direction (i.e., the effect on the drag force is large). The important direction for the lift of the bubble is on the side. On the side of the bubble, the pressure is higher in the wake region. The side pressure is asymmetric because the relative velocity between the liquid and the bubble is slower on the side of B2 in the wake region. The effect of the normal viscous stress on the lateral migration is weak compared to that of the pressure, even though normal viscous stress asymmetry is observed. This shows that the lift, due to pressure asymmetry, acts to help the bubble escape from the original vertical line. The rear pressure nearly coincides at all azimuthal angles. These pressure profiles depend on the tangential velocity. The azimuthal angle velocity has only a small effect.

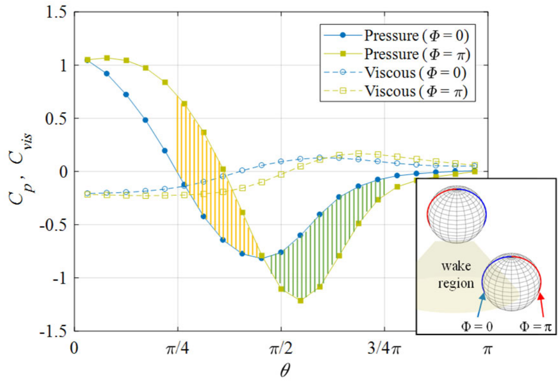

Fig. 10. Asymmetric pressure coefficient C_p and normal viscous stress coefficient C_{vis} of B2 as a function of the angle θ from B2 at $t = 12$. The green area more affects the lift direction than the orange area. Only B2 migrates laterally ($Ga = 40$, $Bo = 1.25$, $\Delta y_0 = 0.1$, Case 7b in Table 1).

In addition, we confirmed a vortex pair behind the bubble. Figure 11 shows the vorticity contour in the z-direction at $t = 12$ in Figure 6. The vorticity, whose effect is negligibly small in the vicinity of B1, is due to the spurious current. Around B2, we find vorticity pairs corresponding to the bubble trajectory. In particular, a pair of counter-rotating threads arises behind the bubble. The liquid evacuation direction according to the counter-rotating thread determines the bubble trajectory. The bubble trajectory corresponding to the counter-rotating threads is the same as that in previous reports of the lift force in a linear shear flow (Magnaudet and Eams 2000) and zigzag motion (Cano-Lozano et al. 2016; Zhang and Ni 2017).

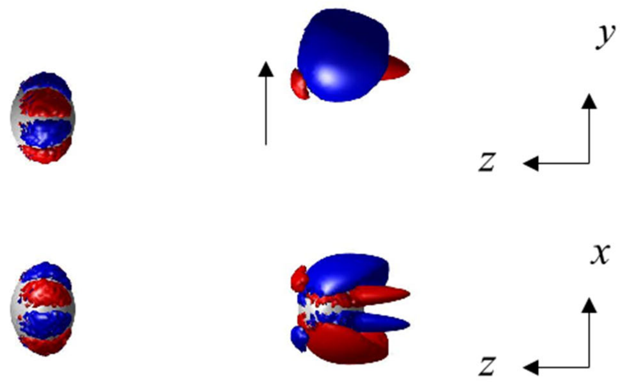

Fig. 11. Isosurface of the vorticity $\omega_z = \pm 0.05$ at t = 12 (Ga = 40, Bo = 1.25, $\Delta y_0 = 0.1$, Case 7b). The arrow shows the direction of the lateral migration of B2.

Quantitative comparisons of the shear-induced lift force are difficult because both the leading and trailing bubbles are deformed; however, qualitative evaluations are possible, i.e., whether the origin of the lift is due to shear or instability. It is known that, when the deformation of a bubble becomes large, the shear-induced lift force becomes opposite to that of a spherical bubble (Adoua et al. 2009; Aoyama et al. 2017). It is expected that lift reversal acts on the bubbles in Case 12 (see Table 1), where the lift coefficient C_L is approximately −0.7 according to the empirical formula of Hayashi et al. (2020). We focus on the direction of the lift force acting on B2 in Case 12.

Figure 12 shows the motions of the bubbles and the vorticity in the z-direction, where B2 is initially positioned a unit radius away from the original vertical line in Case 12b in Table 1. As shown in the figure, lift reversal occurs for B2 and B2 continues to move on the vertical line of B1. The rotation direction of the vorticity pair behind the bubble in Fig. 12 is definitely opposite to that of the spherical-like bubble in Fig.

11.

The above results show that the shear-induced lift force acts on B2 and causes it to escape from the vertical line for spherical-like bubbles under the present conditions. In addition, instability due to the acceleration of B2 rarely occurs. First, it is clear that the lift acting on the bubble is directly related to the vortex pair behind the bubble. When the lift force acts on a spherical bubble in a uniform shear flow, the vortex pair arises behind the bubble because of the stretching/tilting of the vorticity at infinity (Adoua et al. 2009). When the lift acts on a spheroidal bubble with a high aspect ratio in a uniform shear flow, the vortex pair arises because of the tilting of the azimuthal vorticity at the bubble surface and the vortex pair has an opposite sign to that in the case of a spherical bubble. The mechanism of lift reversal is related to the mechanism of instability as a result of infinitesimal disturbances. It is why the unstable region and the lift reversal region nearly coincide. The lift reversal observed in the present study is related to the mechanism of instability, and the wake of B1 uniquely determines the lift direction. Therefore, a spherical trailing bubble escapes from the original vertical line as a result of the shear-induced lift while a spheroidal trailing bubble rarely escapes because of the lift reversal.

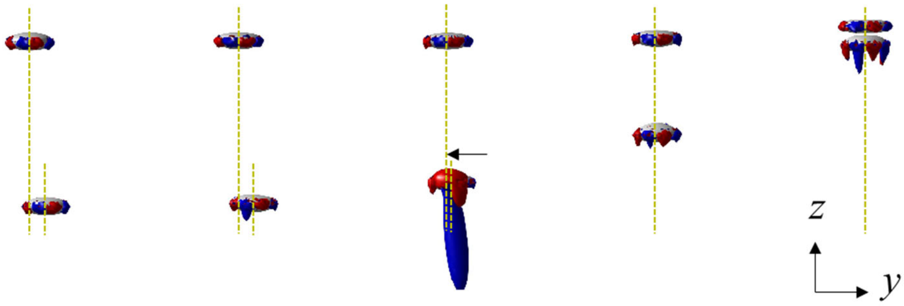

Fig. 12. Isosurface of the vorticity $\omega_z = \pm 0.05$ (Ga = 68, Bo = 8.0, $\Delta y_0 = 0.5$, Case 12b). The arrow shows the direction of the lateral migration of B2.

3.4 Repulsion of the two bubbles

When the bubbles are adjacent, as shown in Figure 5 at time (ii), the bubbles repel each other in opposite horizontal directions. That is, no equilibrium distance is observed. This repulsion interaction acts on both bubbles and is expected from the potential effect because of the small relative distance. First, we use the vertical interaction to discuss why the equilibrium distance is not observed. After explaining the vertical interaction, we then discuss the lateral motion.

Figures 13 shows the pressures and the normal viscous stresses acting on B1 and B2 at time (ii), where $S \sim 2.6$. The rising velocity of B1 increases as a result of an increase in the pressure in the rear part of B1. This is different from the case where the bubbles separate from each other enough to neglect the potential effects. The mechanism of the B1 velocity increase is different from the interaction acting on B2, which increases its rising velocity as the pressure decreases in front of B2 as a result of the wake effect. This is the potential effect.

The interactions acting on B2 include both the potential effect of the decrease in the velocity and the wake effect of the increase in the velocity. Considering the equilibrium distance, the rising velocity needs to decrease as a result of the fore-aft symmetry of the potential flow with the increasing pressure on the front part of B2. However, Figure 13 indicates that the pressure at the front of B2 is less than that of a solitary bubble. Therefore, the rising velocity is also faster than that of B1. The wake effect is larger than the potential effect even when the bubbles are adjacent. This is because the deformation effect is promoted as follows.

- When the bubbles are adjacent, the pressure at the rear of B1 is increased and the aspect ratio is increased (see Figure 8(a)). Therefore, the vorticity generated at the bubble surface increases because of the maximum curvature, as described in Section 3.2.
- The pressure and the relative velocity between the bubble and the liquid in the wake region decrease; therefore, the pressure decreases at the front of B2.
- The pressure in the wake reduces the aspect ratio of B2. As the aspect ratio decreases, the velocity of B2 increases and the bubbles approach each other.

The leading bubble accelerates, and the trailing bubble further accelerates. An equilibrium distance due to the balance between the potential effect and the wake effect is not observed because the wake effect powerfully acts by repeating the above-mentioned effects.

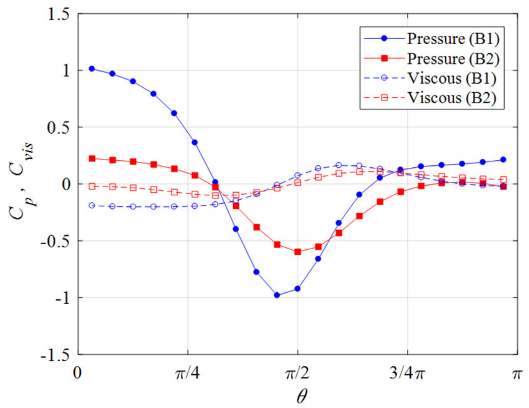

Fig. 13. Pressure coefficient C_p and normal viscous stress coefficient C_{vis} of the bubbles as a function of the angle θ from the center of each bubble at time (ii), the onset of the repulsion of the two bubbles (*Ga* = 40, *Bo* = 1.25, Case 7a in Table 1).

Next, we discuss the factors contributing to the horizontal repulsion. Figure 7(b) shows the lift coefficients of the bubbles. At time (i), the lift coefficient is approximately 0. At time (ii) to (iv), the bubbles repulse apparently. At time (iv), the repulsion is finished and the lift coefficients overshoot for an instant. First, when the potential effect is small at t = 15 prior to the apparent repulsion, lateral migration of B1 is not observed but that of B2 is already observed (see Figure 5(a)). In fact, the curvature asymmetry, which is determined by asymmetric normal stress, can be confirmed first with B2 in Figure 8(c). B2 moves horizontally as a result of the wake effect prior to the horizontal repulsion caused by the potential effect. This lift may result from the flow not being perfectly axisymmetric because of the accumulation of very small numerical errors, such as spatial discreteness, even if the O(Δ^2) error and the center of each bubble varies $(x, y) \neq (0,0)$ during the period of $0 < t < 15$.

Next, when the bubbles approach each other with a small deviation from the original line, the bubbles repel each other horizontally. Figures 14(a) and 14(b) show the pressure coefficient C_p and the normal viscous stress coefficient C_{vis}, respectively, as a function of the angle θ from the center of the bubble surface at time (iii). It is clearly seen that the pressure increases between the bubbles when strong repulsion occurs at time (iii), when $\Phi = 0$ is between the bubbles on the (1, 2) plane (orientation is defined in Figure 4). The repulsion process consists of potential repulsion and lateral migration by the wake with minimal asymmetry. Therefore, repulsion could not be confirmed under weak shear-induced lift conditions, namely low *Ga* or high *Bo* (see Figure 2). For low *Ga*, the lift coefficient is small as a result of the small vorticity in the wake (Eq. (2)) because the viscous effects reduce the tangential velocity at the surface and diffuse the vorticity in the wake, i.e., small vorticity. For high *Bo*, the lift coefficient is small (opposite sign) as a result of deformation. Therefore, horizontal movement due to the wake does not occur. The conditions under which repulsion was observed are strong shear-induced lift and small deformation (the nearly spherical case).

We connect the curvature and the lift coefficient to understand the details of the repulsion. While time (ii) to (iii), the lift coefficient of B1 is greater than that of a spherical model, also greater than B2. We consider that it is a zigzag effect due to the asymmetry curvature. B2 pushes the bottom of B1 at $\phi = 0$, so the B1 at $\phi = 0$ is flattened. The maximum curvature at $\phi = 0$ is greater than that at $\phi = \pi$. Considering the zigzag motion, the bubble moves laterally to the smaller curvature direction. This curvature relationship promotes repulsion (increases lift coefficient). In contrast, the asymmetric curvature of B2 is not so B1 is greater than

B2. At time (iv), the lift coefficients overshoot. It is also a zigzag effect. The curvature of B1 is to the left and right reversed compare to time (iii). It promotes attraction. For a moment, the asymmetric curvature of B2 also promotes attraction.

(a) (b)

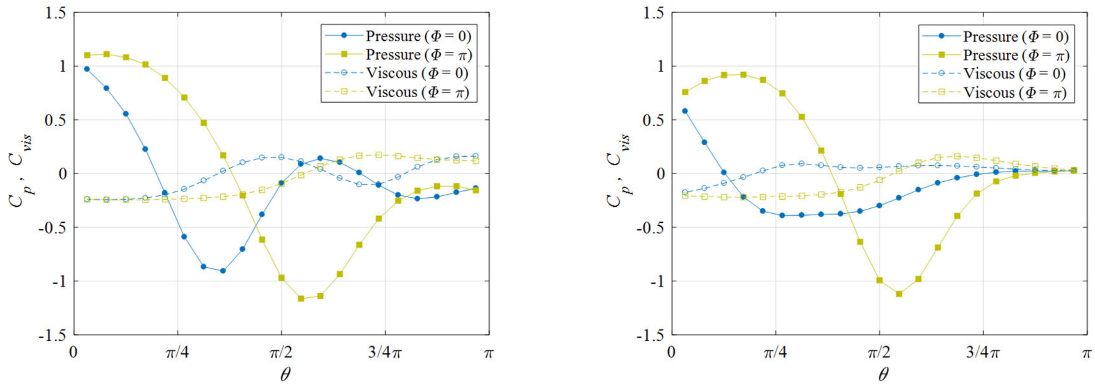

Fig. 14. Asymmetric pressure coefficient C_p and normal viscous stress coefficient C_{vis} as a function of the angle θ from the center of the bubble at time (iii), the maximum repulsion of the two bubbles: (a) B1 and (b) B2.

It is known that counter-rotating threads form behind a bubble when the lift force acts on the bubble. In particular, the vortex structure and the vorticity in the ascending direction are important factors that determine the motion when lift acts on bubbles in a shear flow and when a bubble performs zigzag or spiral motions. For the repulsion, we found an interestingly similar vortex structure. Figure 15 shows the visualized vortex structure, where Figure 15(a) shows the vorticity in the *z*-direction, Figure 15(b) shows the isosurface of $\lambda_2 = -0.001$ (Jeong and Hussain 1995), and Figure 15(c) shows a schematic of the evolution of the vortex orientation. Figure 16 shows an observation of the vortex structure in Figure 15 from a different direction. See also the supplementary movies of Figures 15 and 16. First, at time (i) when B2 accelerates, the characteristic ω_z cannot be confirmed; however, in the visualization using λ_2, a transverse vortex exists on the side of B2. It appears that the transverse vortex is formed by a combination of the acceleration of B2 and the velocity distribution on the side of B2. This vortex becomes a ring-shaped transverse vortex centered on the vertical line of B1, as explained later. At time (i), the counter-rotating threads are not observed.

(a)

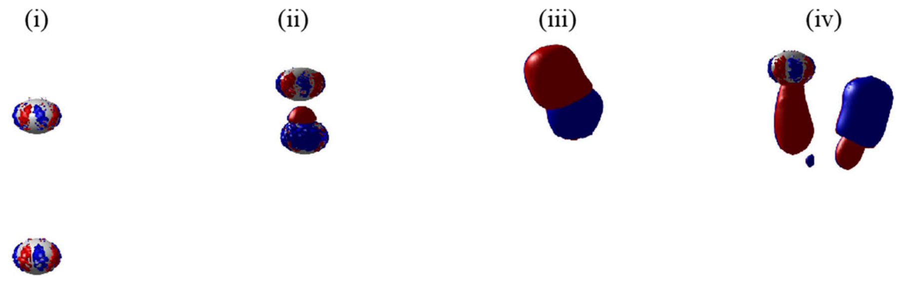

(b)

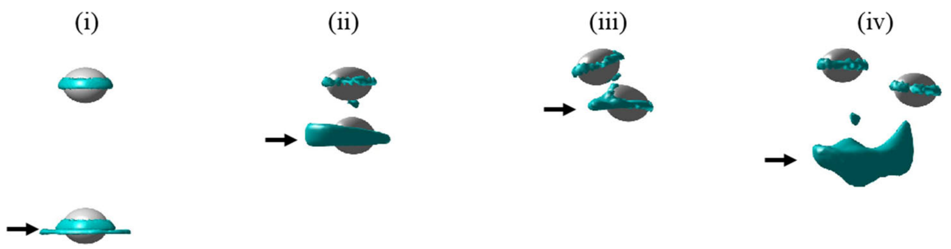

(c)

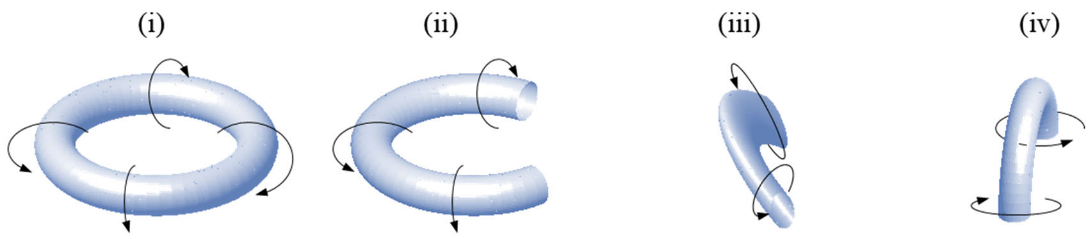

Fig. 15. Vortex structure when the bubbles repel each other corresponding to times (i)–(iv): (a) isosurface

of the vorticity $\omega_z = \pm 0.05$; (b) isosurface of $\lambda_2 = -0.001$; and (c) vortex direction on the side of B2 (the arrows in panel (b)). The vortex ring shifts from transverse to longitudinal because of the velocity profile (see Fig. 17).

(a)

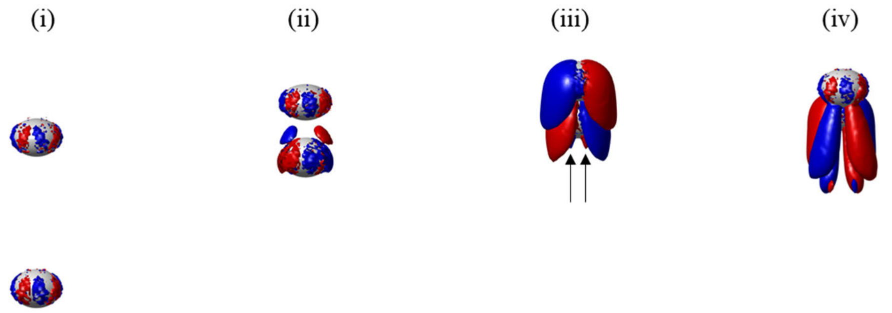

(b)

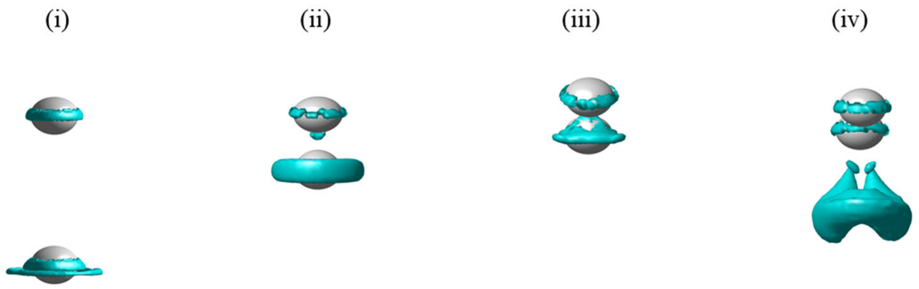

Fig. 16. Another view of Figure 15: (a) isosurface of the vorticity $\omega_z = \pm 0.05$ and (b) isosurface of $\lambda_2 = -0.001$.

Then, when the bubbles start to repel each other at time (ii), a vorticity pair is generated in front of B2. The ω_z pair is aligned in the direction of the motion of the bubbles. The counter-rotating threads are not observed. Later in time, the bubbles approach each other and the vorticity pair in front of B2 connects to the rear of B1. In this way, the evolution of counter-rotating threads behind B1 can be observed (see the details in the movie). For the λ_2 visualization, the ring-shaped vortex becomes asymmetric and the vortex remains inside the wake region of B1.

When the repulsion of the bubbles develops at time (iii), we observe vorticity pairs in both bubbles (the arrows in Figure 16(a), see details in the movie). The signs of the corresponding vorticities behind the two bubbles are opposite, that is, repulsive lift acts on both bubbles. Then, at time (iv), the vorticity pair, which is in front of B1 at time (iii), moves backward. The vorticity pair behind B1 at time (iii) has the opposite sign as that in front of B1 at time (iii); therefore, the sign of the vorticity pair behind B1 at time (iv) is opposite to that behind B1 at time (iii). As a consequence, the lift is estimated to be an attractive force at time (iv) (the lift coefficient overshoots at time (iv) in Figure 7(b)). This series of events appears to be the deformation-dependent lift force seen when the bubbles execute a zigzag motion as a result of the asymmetric curvature. In general, the vorticity pair is generated to move liquid outward because the curvature on the outside is larger than that on the inside as a result of the pressure interaction. The typical induced zigzag motion and the lateral migration of B1 are in agreement. This phenomenon also occurs in B2.

For λ_2, the direction of the vortex structure on the side of B2 begins to change. The vortex structure at time (iv) makes it easier to understand the vortex structure variation at time (iii). A longitudinal vortex is observed behind each bubble at time (iv), which corresponds to the lateral migration at the previous time (iii). The longitudinal vortex generated behind B1 appears to be the ring-shaped transverse vortex that existed on the side of B2 and developed via the potential interaction. Figure 17 shows the tangential velocity profile on the B2 surface for Φ at time (iii). When the potential repulsion occurs, the velocity of $\Phi = 0$ ($\Phi = 0$ is on the (1, 2) plane and between the bubbles) on the side of B2 is the slowest compared to the other Φ values. According to the Φ-dependent velocity, the transverse vortex at $\Phi \neq 0$ moves backward and can become a vertical vortex, as shown in Figure 15(c). Its vortex shift can increase the lift coefficient of B1.

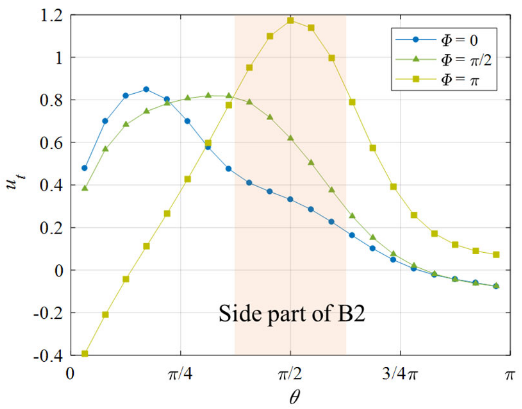

Fig. 17. Tangential velocity profile on the B2 surface for Φ at time (iii) (*Ga* = 40, *Bo* = 1.25, Case 7a in Table 1). The velocity at the side of B2 is slowest for $\Phi = 0$.

The repulsion phenomenon of the bubbles is primarily due to the potential effect and the wake effect with the assumption of a steady condition and spherical bubbles. As described above, however, it is more complicated to interpret the repulsion mechanism of a realistic bubble because of various phenomena such as the deformation of the bubbles, the variation in the added mass, and the time evolution of the vortex interaction. Therefore, it is necessary to examine each phenomenon individually.

4. Summary

The motion of wake-induced approaching bubbles was studied via 3D simulations using a VOF method. The parameters were selected such that the bubbles rose under stable conditions. The bubble–bubble interaction associated with the wake changed as a result of the relative angle and the relative distance between the bubbles. The interactions were qualitatively dependent on the potential effect and the wake effect, as suggested by Hallez and Legendre (2011) assuming spherical bubbles.

The trailing bubble accelerated in response to the wake of the leading bubble, which reduced the pressure in front of the trailing bubble. The trailing bubble velocity increased beyond predictions based on the interaction of spherical bubbles. Deformable bubbles with a large amount of vorticity generation were greatly affected by the pressure reduction. However, the deformation effect corresponding to the relative acceleration may be small because the acceleration mechanism is identical to that of spherical bubbles.

The spherical trailing bubbles migrated laterally from the original line after approaching the leading bubbles, i.e., the bubbles rarely maintained an in-line configuration as a result of the shear-induced lift in the wake. However, oblate bubbles were easily held in the wake as a result of the occurrence of lift reversal (Ga = 68, Bo = 8). The orientations of the longitudinal vortex behind an oblate bubble are opposite to those behind a spherical bubble. These lift mechanisms are completely different; therefore, applying the lift coefficient of a spherical bubble in a wake to an oblate bubble is difficult.

When the trailing bubble was close to the leading bubble, both bubbles migrated laterally in opposite directions as a result of the potential interaction. However, under some weak shear-induced lift conditions, this repulsion rarely occurred as a result of slight path deviations. During the repulsion, the ring-shaped transverse vortex at the side of the trailing bubble became a longitudinal vortex because of the velocity profile around the bubble. The longitudinal vortex affects the lateral migration of the leading bubble, and this effect is complex and includes deformation, added mass, and time evolution. As shown in the presented simulation results, a pair of clean bubbles rising in line behaves in a complicated manner.

Declaration of Competing Interest

The authors declare that they have no known competing financial interests or personal relationships that could have appeared to influence the research reported in this paper.

CRediT authorship contribution statement

Hiroaki Kusuno: Conceptualization, Methodology, Investigation, Data curation, Visualization, Writing-

Original draft. **Toshiyuki Sanada**: Conceptualization, Methodology, Investigation, Writing-Original draft.

Acknowledgments

This work was supported by JSPS KAKENHI, Grant No. 20J13337. The financial support is gratefully acknowledged.

Appendix A. Initial arrangement

This appendix discusses the equilibrium distance of the bubbles (the distance likely deviated from the original line as a result of lateral migration), which varies depending on the initial arrangement observed in the experiment (Watanabe and Sanada 2006). We set $\Delta y_0 = 0.1$ and varied S to simulate the experimental conditions. The relative distance, however, was shorter than that in the experiment because of computational costs.

Figure A1 shows the relative trajectory of the bubbles under the conditions of Case 7 ($Ga = 40$, $Bo = 1.25$). Note that the vertical axis indicates the relative distance and the horizontal axis indicates the relative angle. The symbols indicate whether the bubbles are approaching or not, i.e., the sign of $\partial S/\partial t$. For $\Delta y_0 = 0$, the lateral migration of B2 is not confirmed until the bubbles are adjacent, as shown in Figure 5. Whereas for $\Delta y_0 = 0.1$, which simulates the experiment, the bubbles approach each other and then B2 migrates laterally because of the wake asymmetry. This lateral migration is due to the wake; therefore, the lift force acts immediately even at a large distance. As a consequence, B2 escapes from the original line at a distance corresponding to the initial distance. Furthermore, it escapes from the wake region (approximately on the line in Figure A1, the perturbation velocity is 0.01 on the line as estimated by the model of Hallez and Legendre (2011) in the appendix) and the interaction rarely occurs. Therefore, the equilibrium distance of the experiment is longer than that of the numerical and analytical solutions because the bubbles outside the wake appear to maintain a certain distance.

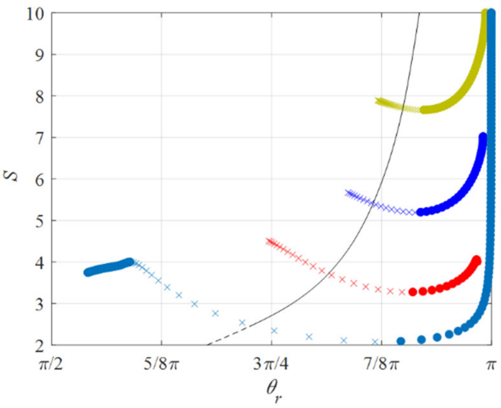

Fig. A1. Relative trajectories for various initial positions, where the symbol “o” indicates that the bubbles are approaching each other, the symbol “x” indicates that the bubbles repel each other, and the dash marks “-” indicate the approximate wake region. Markers are plotted every 0.2 time units.

Appendix B. Size difference

This appendix discusses the relative behavior of the bubbles, which vary depending on the small size difference observed in the experiment (Kusuno et al. 2019). We set $\Delta y_0 = 0.1$ and varied the diameter of B2 by ±5% to simulate the experimental conditions.

Figure B1 shows the relative trajectories of the bubbles under the conditions of Case 7 (*Ga* = 40, *Bo* = 1.25). Note that the vertical axis indicates the relative distance and the horizontal axis indicates the relative angle. When B2 is larger, the bubbles are very close to each other because of the acceleration due to the wake and buoyancy. The lift due to the wake and potential repulsion act on B2, and it migrates laterally. Here, the variation in the relative angle is inversely proportional to the relative distance. The shorter the relative distance, the easier it is to develop asymmetry, i.e., the bubbles shift horizontally in a shorter amount of time. This is why the distance and time at which a bubble escapes from the original line vary with the size dispersibility in the experiment.

As shown in Appendix A, the interaction rarely occurs outside the wake region; therefore, the difference in the buoyancy has a strong effect. It appears that the attractive force acts on B2 when the trailing bubble is larger than the leading bubble and that the repulsive force acts on B2 when the trailing bubble is smaller.

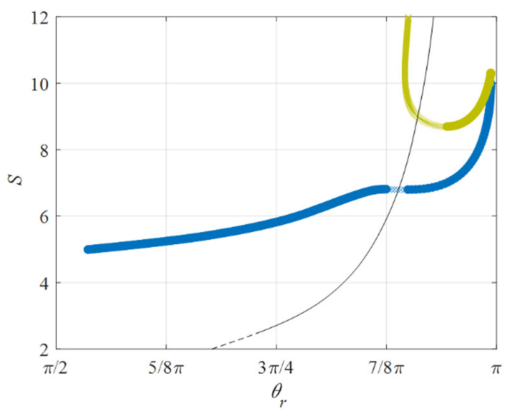

Fig. B1. Relative trajectories for various initial positions, where the symbol “o” indicates that the bubbles are approaching each other, the symbol “x” indicates that the bubbles repel each other, and the dash marks “-” indicate the approximate wake region. Markers are plotted every 0.2 time units.

Appendix C. Tangential velocity and azimuthal vorticity at the bubble surface

This appendix provides the tangential velocity and azimuthal vorticity distribution of both B1 an B2 under the conditions of Case 7 (*Ga* = 40, *Bo* = 1.25) at the time (i) to supplement Sec. 3.2. Figure C1 (a) and (b) show the tangential velocity and azimuthal vorticity, respectively. The tangential velocity of the B2 side (θ = π/2) is lower than that of B1 because of the B1 wake. Consequently, the vorticity is lower because the vorticity generated at the surface proportional to velocity and curvature.

(a) (b)

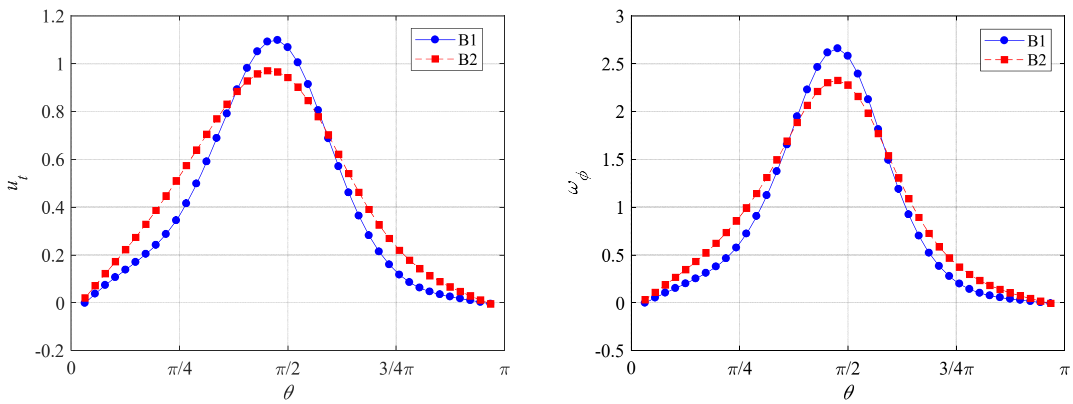

Fig. C1. Tangential velocity and azimuthal vorticity at time (i) corresponding to Figure 5. The velocity of

B2 at the side is lower than that of B1, so the vorticity of B2 is smaller.

Figure C2 shows the maximum vorticity of B1 when the bubbles are far enough apart. The maximum vorticities are positioned to between Eq. (13) and Eq. (14) where the equations are derived in the infinite and low *Re* limit, respectively. It shows that the aspect ratio increases with increasing vorticity. Therefore, the wake effect for B2 increases with the aspect ratio.

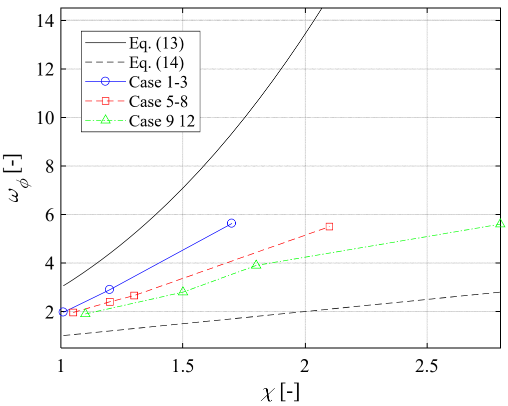

Fig. C2. Maximum azimuthal vorticity of B1. The vorticity increases with increasing the aspect ratio.

References

Adoua, R., Legendre, D., & Magnaudet, J. (2009). Reversal of the lift force on an oblate bubble in a weakly viscous linear shear flow. Journal of Fluid Mechanics, 628, 23-41.

Aoyama, S., Hayashi, K., Hosokawa, S., Lucas, D., & Tomiyama, A. (2017). Lift force acting on single bubbles in linear shear flows. International Journal of Multiphase Flow, 96, 113-122.

Auton, T. R. (1987). The lift force on a spherical body in a rotational flow. Journal of Fluid Mechanics, 183, 199-218.

Batchelor, G. K. (1967). An introduction to fluid dynamics. Cambridge University Press.

Blanco, A., & Magnaudet, J. (1995). The structure of the axisymmetric high-Reynolds number flow around an ellipsoidal bubble of fixed shape. Physics of Fluids, 7(6), 1265-1274.

Cano-Lozano, J. C., Martínez-Bazán, C., Magnaudet, J., & Tchoufag, J. (2016). Paths and wakes of deformable nearly spheroidal rising bubbles close to the transition to path instability. Physical Review Fluids, 1(5), 053604.

De Vries, A. W. G., Biesheuvel, A., & Van Wijngaarden, L. (2002). Notes on the path and wake of a gas bubble rising in pure water. International Journal of Multiphase Flow, 28(11), 1823-1835.

Gumulya, M., Utikar, R. P., Evans, G. M., Joshi, J. B., & Pareek, V. (2017). Interaction of bubbles rising in-line in quiescent liquid. Chemical Engineering Science, 166, 1-10.

Hallez, Y., & Legendre, D. (2011). Interaction between two spherical bubbles rising in a viscous liquid. Journal of Fluid Mechanics, 673, 406-431.

Harper, J. F. (1970). On bubbles rising in line at large Reynolds numbers. Journal of Fluid Mechanics, 41(4), 751-758.

Harper, J. F. (1997). Bubbles rising in line: why is the first approximation so bad? Journal of Fluid Mechanics, 351, 289-300.

Hayashi, K., Legendre, D., & Tomiyama, A. (2020). Lift coefficients of clean ellipsoidal bubbles in linear shear flows. International Journal of Multiphase Flow, 129, 103350.

Howe, M. S. (1995). On the force and moment on a body in an incompressible fluid, with application to rigid bodies and bubbles at high and low Reynolds numbers. The Quarterly Journal of Mechanics and Applied Mathematics, 48(3), 401-426.

Jeong, J., & Hussain, F. (1995). On the identification of a vortex. Journal of Fluid Mechanics, 285(1), 69-94.

Klaseboer, E., Chevaillier, J. P., Maté, A., Masbernat, O., & Gourdon, C. (2001). Model and experiments of a drop impinging on an immersed wall. Physics of Fluids, 13(1), 45-57.

Kochin, N. E., Kibel, I. A., & Roze, N. V. (1964). Theoretical hydrodynamics. Translated from the fifth, Russian ed. by D. Boyanovitch. edited by J.R.M. Radok. New York: Interscience.

Kok, J. W. (1993). Dynamics of a pair of gas bubbles moving through liquid. i: Theory. European Journal of Mechanics B: Fluids, 12(4), 515-540.

Kusuno, H., & Sanada, T. (2020). Velocity distribution in the boundary layer of a bubble rising with a rectilinear motion. Transactions of the JSME, 86(884), 19-00453.

Kusuno, H., Yamamoto, H., & Sanada, T. (2019). Lift force acting on a pair of clean bubbles rising in-line. Physics of Fluids, 31(7), 072105.

Lamb, H. (1945). Hydrodynamics, 6th ed. Dover Publications.

Legendre, D. (2007). On the relation between the drag and the vorticity produced on a clean bubble. Physics of Fluids, 19(1), 018102.

Legendre, D., & Magnaudet, J. (1998). The lift force on a spherical bubble in a viscous linear shear flow. Journal of Fluid Mechanics, 368, 81-126.

Levich, V. G. (1962). Physicochemical hydrodynamics. Prentice Hall.

Magnaudet, J., & Eames, I. (2000). The motion of high-Reynolds-number bubbles in inhomogeneous flows. Annual Review of Fluid Mechanics, 32(1), 659-708.

Magnaudet, J., & Mougin, G. (2007). Wake instability of a fixed spheroidal bubble. Journal of Fluid Mechanics, 572, 311-337.

Moore, D. W. (1963). The boundary layer on a spherical gas bubble. Journal of Fluid Mechanics, 16(2), 161-176.

Mougin, G., & Magnaudet, J. (2002). Path instability of a rising bubble. Physical Review Letters, 88(1), 014502.

Mougin, G., & Magnaudet, J. (2002). The generalized Kirchhoff equations and their application to the interaction between a rigid body and an arbitrary time-dependent viscous flow. International Journal of Multiphase Flow, 28(11), 1837-1851.

Prakash, V. N., Martínez Mercado, J. M., van Wijngaarden, L., Mancilla, E., Tagawa, Y., Lohse, D., & Sun, C. (2016). Energy spectra in turbulent bubbly flows. Journal of Fluid Mechanics, 791, 174-190.

Popinet, S. (2003). Gerris: a tree-based adaptive solver for the incompressible Euler equations in complex geometries. Journal of Computational Physics, 190(2), 572-600.

Popinet, S. (2009). An accurate adaptive solver for surface-tension-driven interfacial flows. Journal of

Computational Physics, 228(16), 5838-5866.

Popinet, S. (accessed on 1 December 2019) Basilisk. http://basilisk.fr/.

Sangani, A. S., Zenit, R., & Koch, D. L. (2001). Measurements of the average properties of a suspension of bubbles rising in a vertical channel. Journal of Fluid Mechanics, 307.

Shew, W. L., Poncet, S., & Pinton, J. (2006). Force measurements on rising bubbles. Journal of Fluid Mechanics, 569, 51-60.

Takagi, S., Ogasawara, T., & Matsumoto, Y. (2008). The effects of surfactant on the multiscale structure of bubbly flows. Philosophical Transactions. Series A, Mathematical, Physical, and Engineering Sciences, 366(1873), 2117-2129.

Tripathi, M. K., Sahu, K. C., & Govindarajan, R. (2015). Dynamics of an initially spherical bubble rising in quiescent liquid. Nature Communications, 6(1), 6268.

Watanabe, M., & Sanada, T. (2006). In-line motion of a pair of bubbles in a viscous liquid. JSME International Journal Series B, 49(2), 410-418.

Yuan, H., & Prosperetti, A. (1994). On the in-line motion of two spherical bubbles in a viscous fluid. Journal of Fluid Mechanics, 278, 325-349.

Zhang, J., & Ni, M. J. (2017). What happens to the vortex structures when the rising bubble transits from zigzag to spiral? Journal of Fluid Mechanics, 828, 353-373.

Zhang, J., Chen, L., & Ni, M. J. (2019). Vortex interactions between a pair of bubbles rising side by side in ordinary viscous liquids. Physical Review Fluids, 4(4), 043604.